Molecular inheritance from cloud to disk: a story of complex organics and accretion shocks

Gelder, M.L. van

Citation

Gelder, M. L. van. (2022, November 24). *Molecular inheritance from cloud to disk: a story of complex organics and accretion shocks*. Retrieved from https://hdl.handle.net/1887/3487189

Chapter 6

Observing accretion shocks with ALMA.

Searching for SO and SO_2 in Class I disks

M. L. van Gelder, A. F. Pérez-Sánchez, B. Tabone, E. F. van Dishoeck

in preparation

Abstract

Context. It remains unknown whether the chemical composition of embedded disks is inherited from their natal envelopes or whether it is reset in a strong accretion shock at the disk-envelope boundary. Both SO and SO_2 have been suggested as good tracers of such accretion shocks.

Aims. We search for accretion shocks with SO and SO_2 in three embedded Class I protostars: TMC1A in Taurus and Ced 110 IRS 4 and IRS 6 in Chameleon.

Methods. Resolved observations with an angular resolution of $\sim 0.15''$ ($\sim$ 10 au radius) taken with the Atacama Large Millimeter/submillimeter Array (ALMA) in Band 6 (1.3 mm) of SO, SO_2, and their isotopologues are investigated. Multiple transitions of SO_2 with a range of $E_{\rm up}$ between $55-119$ K are covered to determine the excitation conditions through LTE modeling of spectra extracted from the peak SO_2 emission.

Results. Both SO and SO_2 are only detected toward TMC1A. The emission is spatially resolved and located around the dust continuum. None of the isotopologues are detected. The SO and SO_2 lines are narrow with a FWHM of 1.0 ± 0.1 km s^{-1}. An excitation temperature of 50 ± 20 K is derived for SO_2 and the column density ratio of SO_2/SO is found to be 0.6 ± 0.1. Other molecules such as c-C_3H_2 and CH_3OH are not detected toward all sources.

Conclusions. An accretion shock origin can be excluded as the origin of the SO and SO_2 emission in TMC1A based on narrow line widths, low excitation temperature, and a comparison of the line ratio to shock models in the literature. Similarly, the lack of SO and SO_2 emission toward IRS 4 and IRS 6 suggests the absence of a strong ($T_{\rm gas,max} > 100$ K) accretion shock. These results imply that the chemical composition of the embedded disks in these sources could be directly inherited from their natal envelopes. Furthermore, the presence of hot SO_2 emission from transitions with $E_{\rm up} > 100$ K seems to be correlated with the bolometric luminosity, suggesting that energetic processes such as ultraviolet irradiation could be important for the formation of SO_2 in the gas phase.

6.1 Introduction

It remains unknown whether the chemical composition of embedded protostellar systems is conserved from envelope to disk (inheritance scenario) or whether it is modified en route (reset scenario). In case of reset, this can be either complete vaporization of all molecules back to atoms with subsequent reformation or a milder form of reset where ices may be sputtered off dust grains and the gas-phase molecular composition may be altered by energetic processes. Some modification to the composition is expected due to the changing temperatures and UV radiation along the infall paths (e.g., Aikawa et al. 1999; Visser et al. 2009; Drozdovskaya et al. 2014). On the other hand, some inheritance is suggested based on the similarities between interstellar and cometary ices (e.g., Mumma & Charnley 2011; Drozdovskaya et al. 2019). A major uncertainty remains whether a strong accretion shock at the disk-envelope boundary may (partially) reset the chemistry. Since planet formation is suggested to start in embedded protostellar disks (e.g., Harsono et al. 2018; Tychoniec et al. 2020), it is important to study such accretion shocks in these young systems to determine their strength and their effect on the chemical composition.

Accretion shocks are commonly seen in models and simulations of infalling envelopes (e.g., Cassen & Moosman 1981; Visser et al. 2009; Li et al. 2013). They are most powerful and result in complete vaporization at early times (Class 0 phase) when accretion occurs close to the star (< 1 au). However, that infalling material ends up in the star and thus does not contribute to the chemical composition of the disk at longer timescales. At later times (Class I phase), accretion occurs further out in the disk (tens of au), with typical shock speeds of a few km s^{-1} impacting gas with densities of $> 10^7$ cm^{-3}. For these conditions, molecules largely survive (i.e., no complete reset) but gas temperatures just behind the shock can reach up to $\gtrsim 1000$ K which drives most of the gaseous oxygen into OH and H_2O. In turn, this leads to enhanced abundances of molecules like SO and SO_2, especially if some ultraviolet (UV) radiation is present (Neufeld & Hollenbach 1994; van Gelder et al. 2021). The dust temperature is also raised, but only to about 50 K, enough to release weakly bound molecules (e.g., CH_4, NH_3) but not strongly bound species like H_2O (Visser et al. 2009; Miura et al. 2017). Some sputtering of ice mantles can also occur.

It is important to observationally constrain the strength of accretion shocks to determine its effect on the disk composition. Common optical shock tracers such as [O I] 6300 Å and [S II] 6371 Å are more sensitive to more energetic shocks in the jet (e.g., Podio et al. 2011; Banzatti et al. 2019; Xie et al. 2021) and are largely extincted in embedded systems by the envelope. For mid-infrared shock tracers such as H_2, H_2O, [S I] 25 μm, and [O I] 63 μm, previous space observatories such as *Spitzer* and *Herschel* lacked the spatial resolution ($5 - 10''$, i.e., suffering from contamination by the outflow; Kristensen et al. 2012; Nisini et al. 2015; Rivière-Marichalar et al. 2016) whereas ground-based observatories suffer from the Earth's atmosphere at infrared wavelengths. The recently launched *James Webb* Space Telescope (JWST) does have both the spatial resolution and sensitivity to disentangle possible accretion shocks from the outflow and jet, but it does not have the spectral resolution to study the kinematics.

At millimeter wavelengths, both SO and SO_2 have been suggested as good tracers of accretion shocks. With the Atacama Large Millimeter/submillimeter Array (ALMA), it is now possible to spatially and kinematically resolve disks and inner envelopes of embedded sources on scales of tens of au, delineating the Keplerian disk (e.g., Tobin et al. 2012; Murillo et al. 2013; Yen et al. 2014; Aso et al. 2017), the entrained outflow and jet (e.g., Arce et al. 2013; Tychoniec et al. 2019; Taquet et al. 2020), and even disk winds down to the launching point in the disk (e.g., Bjerkeli et al. 2016; Tabone et al. 2017). The suitability of SO and SO_2 to trace energetic processes at the disk-envelope interface was demonstrated by the detection of strong SO emission near the centrifugal barrier of the embedded disk around the L1527 Class 0/I protostar (Sakai et al. 2014, 2017). Later, also other detections of SO in possible accretion shocks were found (e.g., the Class I source Elias 29; Oya et al. 2019). Furthermore, strong SO_2 emission was observed related to accretion shocks for a few Class 0 and Class I sources (e.g., Bjerkeli et al. 2019; Artur de la Villarmois et al. 2019). Both SO and SO_2 are also seen at the interface between infalling streamers and disks in more evolved Class II sources (Garufi et al. 2022). However, these two molecules do not exclusively trace accretion shocks but are also seen in outflows (e.g., Codella et al. 2014, 2021; Taquet et al. 2020), disk winds (e.g., Tabone et al. 2017; Lee et al. 2018), or in the warm inner envelopes that are passively heated by the central accreting protostar (e.g., Harsono et al. 2021). Moreover, a strong link between warm SO_2 emission arising from transitions with an upper energy level $E_{\rm up}$ of ~ 200 K with bolometric luminosity was observed (Artur de la Villarmois et al. 2019). The emission therefore has to be carefully compared to sophisticated models of accretion shocks (e.g., Miura et al. 2017; van Gelder et al. 2021) to make robust conclusions about its origin. Moreover, it is important to cover multiple lines of SO and SO_2 with high $E_{\rm up}$ (> 50 K) to exclude emission related to an extended outflow (Tychoniec et al. 2021) and to determine their excitation conditions in order to further characterize the presence of an accretion shock and its strength.

In this work, the presence of accretion shocks is investigated toward three Class I sources: TMC1A in Taurus and Ced 110 IRS 4 and Ced 110 IRS 6 (hereafter IRS 4 and IRS 6) in Chameleon. The main physical properties of these sources are presented in Table 6.1. All three protostars are firmly classified as Class I sources based on their spectral energy distribution (e.g., Evans et al. 2003), compact and warm CO and HCO^+ emission (van Kempen et al. 2009b; Yıldız et al. 2013), outflowing molecular gas (e.g., van Kempen et al. 2009b; Yıldız et al. 2013; Bjerkeli et al. 2016), and the presence of a disk (Pontoppidan & Dullemond 2005; Harsono et al. 2014, 2021).

So far, few Class I sources have been observed with both SO and SO_2. Here, resolved ALMA observations with an angular resolution of $\sim 0.15''$ (~ 10 au radius) of TMC1A, IRS 4, and IRS 6 are presented covering two transitions of SO and five transitions of SO_2 with a range of $E_{\rm up}$ between $55 - 119$ K which allow for determining their excitation conditions. Additionally, several transitions of the optically thin $S^{18}O$, $^{34}SO_2$, $^{33}SO_2$, and $SO^{18}O$ isotopologues are also covered. In Sect. 6.2, the ALMA observations are detailed. The results are presented in

Table 6.1: Main physical properties of the three Class I sources discussed in this paper.

Source	RA (J2000) (hh:mm:ss.ss)	Dec (J2000) (dd:mm:ss.s)	d (pc)	L_{bol} ($\mathrm{L}_{\odot}$)	T_{bol} (K)	M_{env} ($\mathrm{M}_{\odot}$)
TMC1A	04:39:35.21	25:41:44.1	140(1)	2.7(2)	118(2)	0.2(2)
Ced 110 IRS 4	11:06:46.37	-77:22:32.9	190(3)	1.0(4)	72(4)	0.07(5)
Ced 110 IRS 6	11:07:09.58	-77:23:05.0	190(3)	0.8(4)	260(4)	0.04(5)

Notes. The coordinates are those of the peak 1.3 mm continuum emission.
(1) Torres et al. (2007). (2) Kristensen et al. (2012). (3) Dzib et al. (2018a). (4) Lehtinen et al. (2001). (5) van Kempen et al. (2009b).

Sect. 6.3 and discussed in Sect. 6.4. Lastly, our conclusions are presented in Sect. 6.5.

6.2 Observations

The data of this work are taken with the 12m array of ALMA in Band 6 under the program 2021.1.01322.S (PI: M.L. van Gelder) with the aim of detecting multiple transitions of SO and SO_2 and their isotopologues (e.g., $S^{18}O$, $^{34}SO_2$), see Table 6.C.2 for a full list of the targeted transitions. The main technical properties of these data are listed in Table 6.C.1. TMC1A was observed in June 2022 in ALMA configuration C-6 with a angular resolution of $0.20{\times}0.15''$ ($\sim$ 10 au radius). The two Cederblad sources were observed in November 2021 in ALMA configuration C-7 with a synthesized beam of $0.16{\times}0.10''$ ($\sim$ 10 au radius). The spectral resolution of all spectral windows are 0.15 km s^{-1} except for a continuum window which has a spectral resolution of 1.3 km s^{-1}. The line sensitivity over 0.15 km s^{-1} is 2.3 K and 4.5 K for TMC1A and the two Chameleon sources, respectively.

The TMC1A data are pipeline calibrated and imaged with the Common Astronomy Software Applications[1] (CASA; McMullin et al. 2007) version 6.2.1.7. For the two Chameleon sources, the data are manually calibrated and imaged with CASA version 5.1.1. Continuum images are made from line-free channels. Following continuum subtraction in the *uv*-plane using the UVCONTSUB task of CASA, line images are made using a mask size that incorporates all the line emission with the TCLEAN task using a Briggs weighting of 0.5. The resulting continuum images are presented in Fig. 6.1 and integrated intensity maps of the SO $6_5 - 5_4$ (E_{up} = 50.7 K) and SO_2 $13_{1,13} - 12_{0,12}$ (E_{up} = 82.2 K) lines are presented in Fig. 6.2. Spectra presented in this work are extracted from the peak of the integrated SO_2 $13_{1,13} - 12_{0,12}$ emission in Fig. 6.2 for TMC1A and from the peak of the continuum emission for IRS 4 and IRS 6 since no 3σ detections in SO_2 are present.

---

[1] `https://casa.nrao.edu/`

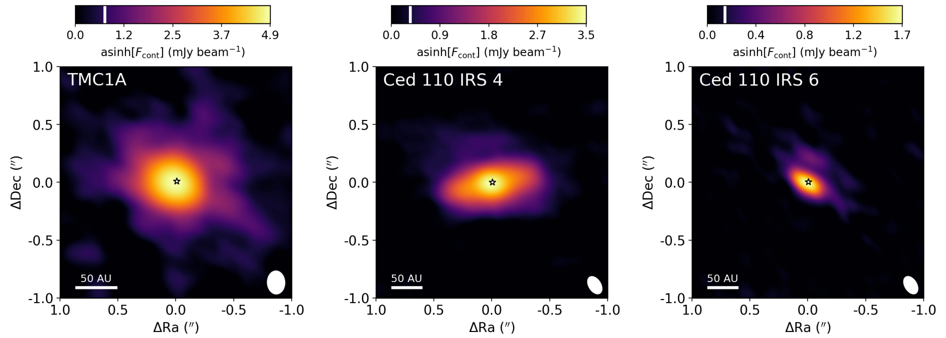

Figure 6.1: The 1.3 mm continuum emission of TMC1A (left), IRS 4 (middle), and IRS 6 (right). All images are shown with an asinh stretch to enhance fainter features without over-saturating bright emission (e.g., Andrews et al. 2018). For each map, a colorbar is displayed on top where the $3\sigma_{\rm cont}$ level is indicated with the white bar (see Table 6.C.1 for $\sigma_{\rm cont}$ values). The peak of the continuum emission is highlighted with the star. The size of the synthesized beam is displayed in the bottom right of each image and on the bottom left a 50 au scale bar is shown.

6.3 Results

6.3.1 Dust continuum

The 1.3 mm continuum emission maps of the three sources studied in this work are presented in Fig. 6.1. In all three sources, a disk-like structure in the continuum is evident. For TMC1A, the disk was already kinematically confirmed from CO isotopologues ($\sim$ 100 au in radius; Harsono et al. 2014). Later, that dust disk was also spatially resolved in high-angular resolution ALMA observations of both the dust continuum and molecular emission ($\sim$ 30 au in radius; Harsono et al. 2021). For both IRS 4 and IRS 6, these are the first data where the continuum is spatially resolved. The dust disks of IRS 4 and IRS 6 are large with radii of about $\sim$ 75 au and $\sim$ 50 au, respectively. Interestingly, IRS 6 also shows some continuum emission toward the north, pointing toward a possible binary companion. If this emission indeed originates from a companion, the separation would be about $\sim$ 40 au and the companion would have a dust disk of $\lesssim$ 25 au in radius.

The total dust mass in these disks, $M_{\rm disk,dust}$, can be estimated using the equation of Hildebrand (1983),

$$M_{\rm disk,dust} = \frac{F_{\rm cont} d^2}{\kappa_\nu B_\nu(T_{\rm dust})}, \tag{6.1}$$

with $F_{\rm cont}$ the disk integrated continuum flux, B_ν the Planck function for a given dust temperature, $T_{\rm dust}$, and κ_ν the dust opacity in the optically thin limit. The disk integrated continuum flux is computed through Gaussian fitting with the CASA task IMFIT. A dust temperature of 30 K is assumed, which is typical for the inner envelopes of embedded protostellar systems (Whitney et al. 2003). The

Table 6.2: Disk integrated continuum fluxes and disk masses computed for our three Class I sources.

Source	$F_{1.3\mathrm{mm}}$ (mJy)	M_{disk} ($\mathrm{M}_\odot$)	$M_{\mathrm{disk}}/M_{\mathrm{env}}$
TMC1A	170 ± 34	$1.4 \pm 0.3(-2)$	$7.1 \pm 1.4(-2)$
Ced 110 IRS 4	64 ± 13	$9.8 \pm 2.0(-3)$	$1.4 \pm 0.3(-1)$
Ced 110 IRS 6	4.4 ± 0.9	$6.7 \pm 1.3(-4)$	$1.7 \pm 0.3(-2)$

Notes. $a(b)$ represents $a \times 10^b$. The total disk mass M_{disk} is computed the dust disk mass $M_{\mathrm{disk,dust}}$ using Eq. (6.1) and multiplying this by a gas-to-dust mass ratio of 100.

dust opacity, κ_ν, is set to 2.3 cm^2 g^{-1} for a wavelength of 1.3 mm (e.g., Ansdell et al. 2016). Following this, the total disk mass M_{disk} is calculated by multiplying $M_{\mathrm{disk,dust}}$ with a gas-to-dust mass ratio of 100. An error of 20% is assumed on F_{cont} which is propagated to M_{disk}. The calculated values for F_{cont}, M_{disk}, and $M_{\mathrm{disk}}/M_{\mathrm{env}}$ are reported in Table 6.2.

In all three sources, the envelope masses are higher than those of their disks, further proving the embedded nature of these sources. The disk mass of TMC1A is the largest within our sample and agrees within a factor 3 with that derived by Harsono et al. (2014) due a difference in the assumed κ_ν. IRS 4 hosts a disk with a similar mass, but its $M_{\mathrm{disk}}/M_{\mathrm{env}}$ ratio is higher than that of TMC1A. The disk in IRS 6 has the lowest mass of our sample as well as the lowest $M_{\mathrm{disk}}/M_{\mathrm{env}}$.

6.3.2 SO and SO$_2$

In Fig. 6.2, the integrated intensity maps of SO $6_5 - 5_4$ (E_{up} = 50.7 K) and SO$_2$ $13_{1,13} - 12_{0,12}$ (E_{up} = 82.2 K) are presented. Both SO and SO$_2$ are only detected toward TMC1A; IRS 4 and IRS 6 do not show emission from any molecule targeted within our observations. Only the $6_5 - 5_4$ transition of SO is detected toward TMC1A, the $2_1 - 1_2$ transition (E_{up} = 15.8 K) is not detected although this may largely be due to a low intrinsic line strength ($A_{\mathrm{ij}} = 1.4 \times 10^{-6}$ s^{-1} versus 1.9×10^{-4} s^{-1} for the $6_5 - 5_4$ transition). The SO $6_5 - 5_4$ transition is the same line as was targeted by Harsono et al. (2021) and therefore shows the same emission morphology but with a factor three higher . Interestingly, the SO$_2$ emission seems to peak at a similar location as SO in TMC1A, to the south west of the continuum emission. However, the emission of SO$_2$ is more compact than that of SO, although this may possibly be limited by the sensitivity. Two other transitions of SO$_2$ with E_{up} of 55 and 94 K are also detected at a similar position as the SO$_2$ $13_{1,13} - 12_{0,12}$ line in Fig. 6.2. The two SO$_2$ transitions with $E_{\mathrm{up}} > 100$ K are not detected. Other molecules targeted within the program, such as c-C$_3$H$_2$ and CH$_3$OH, are not detected toward any of the sources, see Appendix 6.A.

To determine the amount of SO and SO$_2$ in TMC1A, a spectrum is extracted from the peak pixel of the SO$_2$ emission in Fig. 6.2. Using the spectral analysis

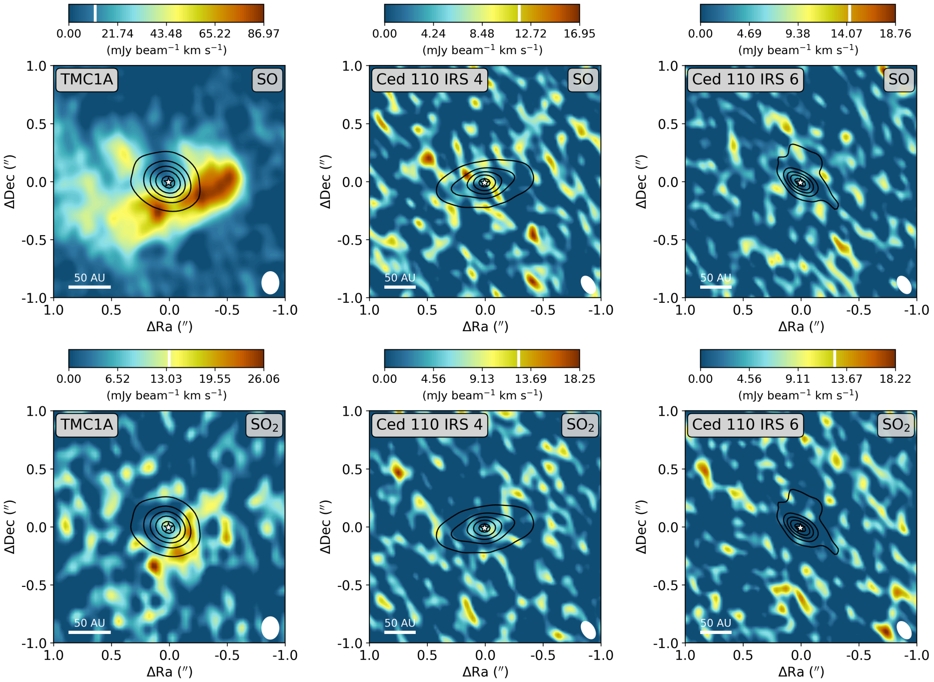

Figure 6.2: Integrated intensity maps of SO $6_5 - 5_4$ ($E_{\rm up} = 50.7$ K, top row) and SO$_2$ $13_{1,13} - 12_{0,12}$ ($E_{\rm up} = 82.2$ K, bottom row) of TMC1A (left), IRS 4 (middle), and IRS 6 (right). The images are integrated over [-5,5] km s^{-1} with respect to the $V_{\rm lsr}$. The color scale is shown on the top of each image, where the white bar indicates the $3\sigma_{\rm line}$ level. The continuum flux is overplotted with the black contours at [0.1,0.3,0.5,0.7,0.9] times the peak continuum flux of 67.5, 17.3, and 2.5 mJy beam^{-1} for TMC1A, IRS 4, and IRS 6, respectively. The peak of the continuum emission is highlighted with the star. The size of the synthesized beam is displayed in the bottom right of each image and on the bottom left a scale bar is shown.

tool CASSIS[2] (Vastel et al. 2015) and assuming local thermodynamic equilibrium (LTE), a column density and excitation temperature are determined for SO$_2$ by using the grid fitting method of van Gelder et al. (2020). For SO, only one transition is detected and therefore the excitation temperature is fixed to that derived for SO$_2$. The line lists of SO and SO$_2$ are taken from the CDMS catalog[3] (Müller et al. 2001, 2005; Endres et al. 2016). Since the emission is resolved, the source size is set equal to the beam size (i.e., beam dilution = 1). The critical densities of the SO and SO$_2$ lines lie around $\sim 10^6$ cm^{-3}, indicating that non-LTE effects will contribute only if the inner envelopes have low density.

The best-fit model to the SO$_2$ lines of TMC1A is presented in Fig. 6.3. For SO$_2$, the best-fit column density and excitation temperature are $7.1 \pm 0.8 \times 10^{14}$ cm^{-2}

---

[2] `http://cassis.irap.omp.eu/`

[3] `https://cdms.astro.uni-koeln.de/`

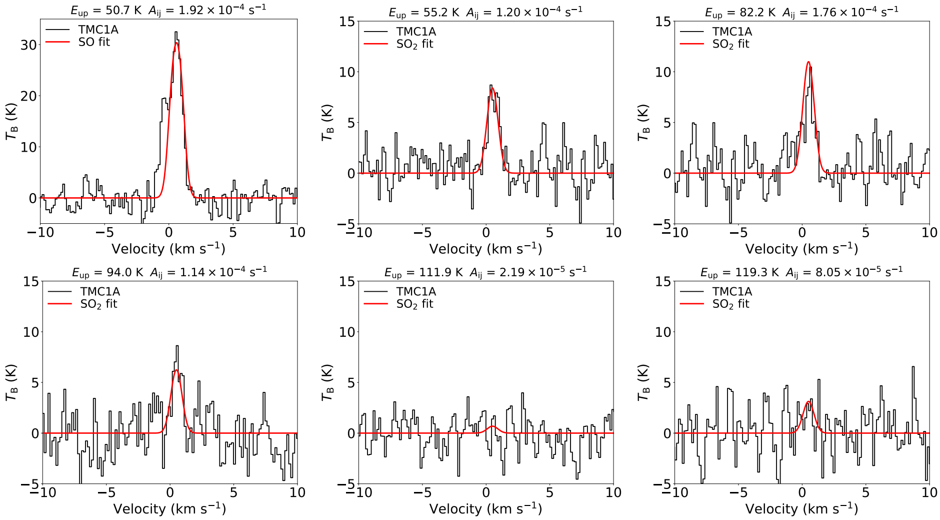

Figure 6.3: Spectrum of TMC1A (in black) centered around the SO 6_5-5_4 (top left) and five SO_2 transitions (other five panels). The $E_{\rm up}$ and $A_{\rm ij}$ of the corresponding transitions are reported on the top of each panel. The best-fit LTE model is overlayed on top in red. For SO_2, the two lines with $E_{\rm up} > 100$ K (bottom middle and right panels) are considered non-detections.

and 50 ± 20 K, respectively. For SO, a column density of $1.1 \pm 0.2 \times 10^{15}$ cm^{-2} is derived for an excitation temperature of 50 K. This is about a factor 2-3 higher than that of Harsono et al. (2021) which was computed over the full disk and assuming that $T_{\rm ex} = 30$ K. The observed column densities give a ratio of SO_2/SO of 0.6 ± 0.1. The SO $6_5 - 5_4$ line is optically thick with $\tau_{\rm line} > 1$. For most of the SO_2 lines, $\tau_{\rm line} \sim 0.2$, indicating that the emission of SO_2 is marginally optically thick. Unfortunately, none of the isotopologues (in particular $S^{18}O$ and $^{34}SO_2$) are detected to test the optical depth and the limits that can be placed from their non-detections do not provide stringent constraints. The derived excitation temperature of SO_2 of 50 ± 20 K is the same as the rotational temperature $T_{\rm rot}$ found using the traditional rotational diagram analysis (Goldsmith & Langer 1999).

Both SO and SO_2 show narrow lines toward TMC1A with a FWHM of 1.0 ± 0.1 km s^{-1} at a $V_{\rm lsr}$ of 7.1 ± 0.1 km s^{-1}. It is important to note that the spectrum is extracted from a single position within the disk; the disk integrated spectrum shows broader lines at different velocities due to the rotation of the disk and envelope. However, the main interest here is to derive a ratio between SO and SO_2 at a single (possibly shocked) position rather than an integrated column over the full disk.

For IRS 4 and IRS 6, only upper limits can be derived for both SO and SO_2. Assuming an excitation temperature of 50 K and a FWHM of 1 km s^{-1}, the 3σ upper limits on the column densities are 3×10^{14} cm^{-2} and 7×10^{14} cm^{-2} for SO and SO_2, respectively. The spectra of IRS 4 and IRS 6 and are presented in Appendix 6.B.

6.4 Discussion

6.4.1 Inheritance vs reset: constraining the shock strength

Both SO and SO_2 are commonly observed toward shocked regions, either in outflows or jets (e.g., Codella et al. 2014; Taquet et al. 2020) but also in disk winds (e.g., Tabone et al. 2017; Lee et al. 2018). In shocks, these molecules typically show broad lines (> 5 km s^{-1}) originating from high-$E_{\rm up}$ transitions (> 100 K). However, emission from either of these two molecules does not directly imply a shocked origin. In earlier observations of TMC1A, the emission of SO was attributed to the inner envelope that is passively heated by the central protostar (Harsono et al. 2021). To determine whether the SO and SO_2 emission is indeed related to an accretion shock, it is important to compare their excitation conditions and column density ratio to sophisticated shock models of low-velocity (< 10 km s^{-1}) in high-density ($> 10^6$ cm^{-3}) environments (e.g., Miura et al. 2017; van Gelder et al. 2021).

For TMC1A, our derived column density ratio of SO_2/SO of 0.6 ± 0.1 is high compared to what is presented in the shock models of van Gelder et al. (2021), see Fig. 6.4. In the presence of a strong UV field (> 100 times higher than that in the ISM; Mathis et al. 1983), it could imply either a high-velocity (> 6 km s^{-1}) shock in a high-density ($> 10^7$ cm^{-3}) environment or a low-velocity shock (< 4 km s^{-1}) at lower densities ($< 10^6$ cm^{-3}). If the UV field similar to that of the ISM, it would imply either a low-velocity (< 2 km s^{-1}) or high-velocity (> 6 km s^{-1}) shock in a low-density ($< 10^6$ cm^{-3}) environment. In the absence of a UV field, the abundances of SO and in particular SO_2 barely increase in accretion shocks (van Gelder et al. 2021). Similarly, when a sufficiently high magnetic field is present so that the accretion shock is of C-type, no increase in SO and SO_2 abundance is present and the length of the shock approaches envelope scales (> 1000 au). In such cases, the SO_2/SO ratio represents that of the abundance ratio in the gas of the infalling envelope.

A high-velocity (> 5 km s^{-1}) shock can be excluded as the origin of the SO and SO_2 emission in TMC1A given that the lines of both SO and SO_2 are narrow (1.0 ± 0.1 km s^{-1}) and that a low excitation temperature of 50 ± 20 K is derived for SO_2. If the emission does arise from an accretion shock, the density is low ($< 10^6$ cm^{-3}) and the shock propagates at low velocities (< 2 km s^{-1}). A hot core origin is also not likely given that the SO_2/SO ratio observed toward the hot core IRAS 16293-2422 is higher ($\gtrsim 3$; Drozdovskaya et al. 2018) and also because CH_3OH is not detected (see Appendix 6.A). A more likely explanation for the origin of SO and SO_2 in TMC1A is the warm inner envelope that is passively heated by the central protostar (Harsono et al. 2021).

For the two Chameleon sources, the lack of SO and SO_2 emission is a strong indication of a weak (less than that in the ISM) UV field. If a UV field is still present, the velocity of the shock can be constrained to be < 2 km s^{-1} in case of a weakly magnetized environment (J-type) and < 7 km s^{-1} in case of a stronger magnetic fields (C-type).

The absence of clear shocked SO and SO_2 emission at the disk-envelope bound-

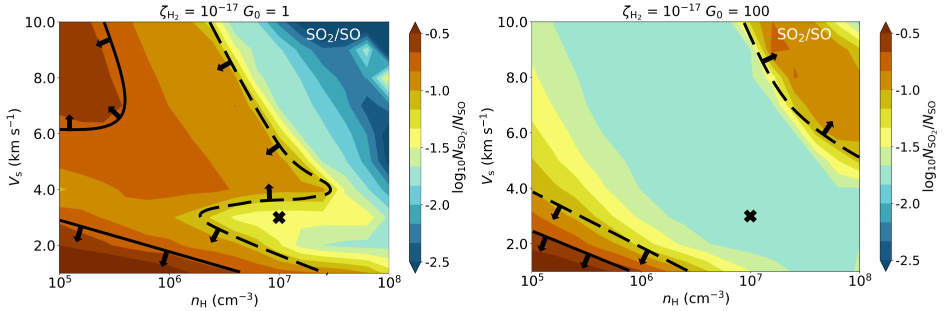

Figure 6.4: Column density ratios of $\mathrm{SO_2/SO}$ in the shock models of van Gelder et al. (2021, their Figure 10) as function of pre-shock density n_H and shock velocity V_s for a UV-radiation field equal to the ISM (left) and 100 times stronger than the ISM (right). A colorbar is displayed on the right of each panel and the black cross indicates their fiducial model. The black solid contours in each panel highlight the region in the parameter space where the observed column density ratio of TMC1A ($\log_{10} N_{\mathrm{SO_2}}/N_{\mathrm{SO}} = -0.3$) agrees with the models. The dashed black contours mark a region where the observed ratio agrees with the models within a factor of 3.

aries of these three sources indicates that either no accretion shocks are present or that the shocks are weak with temperatures of < 100 K (i.e., too low to trigger gas-phase formation or thermal desorption of SO and $\mathrm{SO_2}$ Miura et al. 2017; van Gelder et al. 2021). This implies that the chemical composition of the envelope material that accretes onto these disks remains intact. In turn, this suggests that any planets forming in these three disks may directly inherit the chemical composition from their natal envelopes. A caveat in this conclusion is that most of the mass in the disk which remains there (i.e., does not directly fall onto the central star) is likely accreted in the late Class 0 and early Class I phases (e.g., Visser et al. 2009; Cridland et al. 2022). All three sources are Class I sources with still significant accretion occurring onto their disks (Pontoppidan & Dullemond 2005; van Kempen et al. 2009b; Aso et al. 2015). Accretion shocks could have existed in earlier stages which did (partially) affect the chemical composition entering the disk.

6.4.2 Relation between warm $\mathrm{SO_2}$ and source properties

Despite the fact that the SO and $\mathrm{SO_2}$ emission is not related to accretion shocks in the three sources studied here, a link between their presence and source properties such as L_bol and T_bol may still be present (e.g., Artur de la Villarmois et al. 2019). In Fig. 6.5, our sources are plotted as a function of L_bol and T_bol, indicating whether or not SO and $\mathrm{SO_2}$ emission is present. A distinction is made between sources where hot $\mathrm{SO_2}$ (transitions with $E_\mathrm{up} > 100$ K) is detected or if only cold $\mathrm{SO_2}$ ($E_\mathrm{up} < 100$ K) is present. Besides our sources, also sources from the literature where SO and $\mathrm{SO_2}$ are probed on disk scales (i.e., not in an outflow or jet) are presented in Fig. 6.5.

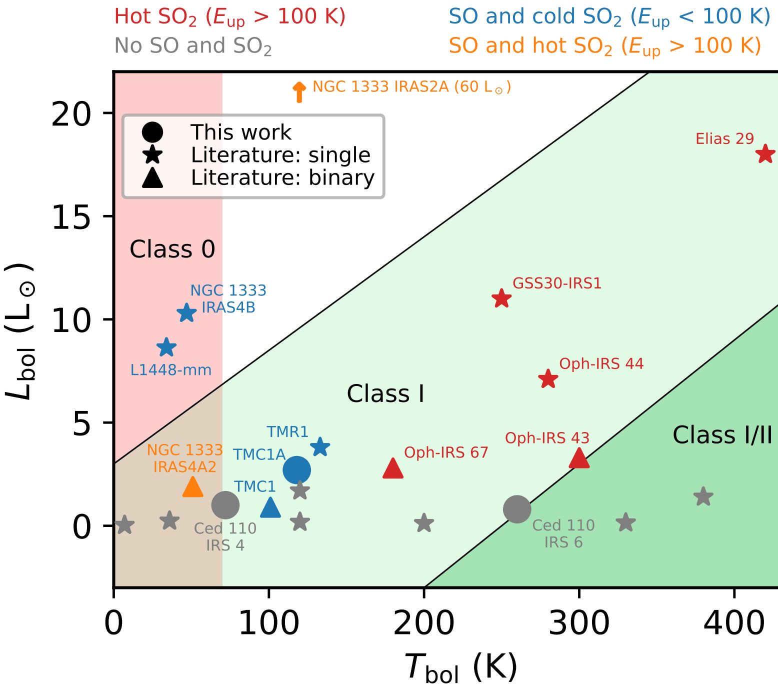

Figure 6.5: The presence of SO and SO$_2$ emission as function of the source properties L_{bol} and T_{bol} (updated version of Fig. 13 in Artur de la Villarmois et al. 2019). Besides the sources in this work (circles), also single sources (stars) and binary sources (triangle) from the literature are included (Artur de la Villarmois et al. 2019; Yang et al. 2021). With colors, a distinction is made between the detection of SO and hot SO$_2$ (transitions with $E_{up} > 100$ K) in orange, SO and cold SO$_2$ (only transitions with $E_{up} < 100$ K) in blue, hot SO$_2$ and no information in the literature on SO (red), and absence of both SO and SO$_2$ (gray). The shaded colors in the background indicate the empirical characterization of Class 0 (pink), Class I (light green), and more evolved Class I and Class II sources (dark green) based on the line emission of SO$_2$ and C^{17}O (Artur de la Villarmois et al. 2019).

First, it is evident that all sources with $L_{bol} > 2$ L$_\odot$ show emission from either SO or SO$_2$. Interestingly, all sources showing emission from hot SO$_2$ lines ($E_{up} > 100$ K) are either single or binary sources with high $L_{bol} > 5$ L$_\odot$ (GSS30-IRS1, Oph-IRS 44, Elias 29, NGC 1333 IRAS 2A) or binaries with moderate $L_{bol} \sim 3$ L$_\odot$ (Oph-IRS 43, Oph-IRS 67, and NGC 1333 IRAS 4A2 Artur de la Villarmois et al. 2019; Yang et al. 2021). This trend was attributed to SO$_2$ tracing high-energetic processes possibly linked to high accretion rates (Artur de la Villarmois et al. 2019). For all the sources with hot SO$_2$, an accretion shock origin has not been excluded. Second, sources which only show cold SO$_2$ (and SO) are either younger Class 0 sources with higher $L_{bol} > 7$ L$_\odot$ or Class I sources with lower $L_{\rm bol} < 5$ L$_\odot$. Among these sources is TMC1A, for which an accretion shock origin of the SO_2 emission is excluded. The other two Class I sources in this category are TMR1 (Harsono et al. 2014) and the binary TMC1 (Harsono et al. 2014; Tychoniec et al. 2021). The reason that the Class 0 sources show only cold SO_2 could be related to their higher envelope mass than Class I sources. The energetic radiation from a Class 0 protostar is absorbed close to the protostar (and re-emitted at longer wavelengths) leading to a cold envelope and low $T_{\rm bol}$ whereas more evolved Class I sources with the same $L_{\rm bol}$ have less massive envelopes leading to more energetic radiation at larger scales leading to higher $T_{\rm bol}$ and thus warmer SO_2. Lastly, sources that do not show any emission of both SO and SO_2 all have low $L_{\rm bol} < 2$ L$_\odot$. Both the Chameleon sources studied in this work fall in this category. These sources are likely cold with little energetic processes to form or excite any SO and SO_2 in the gas phase.

This summary shows that high $L_{\rm bol}$ is necessary for SO and especially SO_2 to be formed in (or desorbed into) the gas phase. For the latter, a higher luminosity also leads to detections of more excited transitions. Low-mass protostars are known to undergo accretion outbursts in their embedded stages roughly every 5000-10 000 years where their luminosities can increase significantly (e.g., Jørgensen et al. 2015; Hsieh et al. 2019; van 't Hoff et al. 2022). Given the sensitivity of the chemistry of SO and SO_2 to the strength of the UV field (e.g., van Gelder et al. 2021), accretion shocks may therefore possibly be best traced by these molecules in outbursting and sufficiently luminous sources.

6.5 Conclusions

In this work, resolved ALMA observations with an angular resolution of $\sim 0.15''$ ($\sim$ 10 au radius) of SO and SO_2 are presented of three embedded Class I protostellar systems: TMC1A, Ced 110 IRS 4, and Ced 110 IRS 6. Both SO and SO_2 are only detected toward TMC1A and spectra are extracted from the peak pixel of SO_2 $13_{1,13} - 12_{0,12}$ ($E_{\rm up} = 82.2$ K) emission. From the multiple SO_2 lines with a range of $E_{\rm up}$ between $55 - 119$ K, the excitation temperature of SO_2 is derived to be $\sim 50 \pm 20$ K. All lines from both SO and SO_2 are narrow with a FWHM of 1.0 ± 0.1 km s^{-1}. An SO_2/SO column density ratio of 0.6 ± 0.1 is found.

Based on the low excitation temperature, narrow lines, and a comparison to sophisticated shock models, an accretion shock origin of the SO and SO_2 emission in TMC1A is excluded. Similarly, the absence of SO and SO_2 emission toward IRS 4 and IRS 6 indicates that no strong accretion shock is present at the disk-envelope boundary of these sources. These results imply that the chemical composition of their disks could be inherited from the natal envelopes with little reprocessing due to accretion shocks.

Emission of hot SO_2 (transitions with $E_{\rm up} > 100$ K) is only present in single sources with high luminosities ($L_{\rm bol} > 5$ L$_\odot$) or binary sources with moderate luminosities ($L_{\rm bol} \sim 3$ L$_\odot$). Furthermore, all sources that do not have SO and SO_2 emission have low luminosities ($L_{\rm bol} < 2$ L$_\odot$). Given that a higher $L_{\rm bol}$ is related to more energetic radiation (i.e., stronger UV field), this suggests that energetic processes are important for the formation of SO_2 in the gas phase.

These results advocate that strong accretion shocks are not universal in embedded protostellar systems, at least not at the Class I stage, and that for these three sources the chemical composition in their disks could be directly inherited from their natal envelopes. Future observational studies of more embedded systems such as the ALMA programs 2022.1.00209.S (PI: E. Artur de la Villarmois) and 2022.1.01411.S (PI: M.L. van Gelder) will provide a larger statistical sample of Class I sources with or without strong accretion shocks to determine their relevance. Moreover, several JWST programs (i.e., 1290 and 1960: PI: E.F. van Dishoeck) with both the NIRSpec and MIRI instruments will provide data of near and mid-infrared shock tracers such as H_2, H_2O, OH, [S I] 25 μm. These will clearly reveal the current hot spots in protostellar systems and can be combined with SO and SO_2 of ALMA to further constrain the presence and strength of accretion shocks.

Acknowledgments

The authors acknowledge acknowledge assistance from Allegro, the European ALMA Regional Center node in the Netherlands. This paper makes use of the following ALMA data: ADS/JAO.ALMA#2021.1.01322.S. ALMA is a partnership of ESO (representing its member states), NSF (USA) and NINS (Japan), together with NRC (Canada), MOST and ASIAA (Taiwan), and KASI (Republic of Korea), in cooperation with the Republic of Chile. The Joint ALMA Observatory is operated by ESO, AUI/NRAO and NAOJ. Astrochemistry in Leiden is supported by the Netherlands Research School for Astronomy (NOVA), by funding from the European Research Council (ERC) under the European Union's Horizon 2020 research and innovation programme (grant agreement No. 101019751 MOLDISK), and by the Dutch Research Council (NWO) grant TOP-1 614.001.751. Support by the Danish National Research Foundation through the Center of Excellence "InterCat" (Grant agreement no.: DNRF150) is also acknowledged.

Appendix

6.A Maps of c-C_3H_2 and CH_3OH

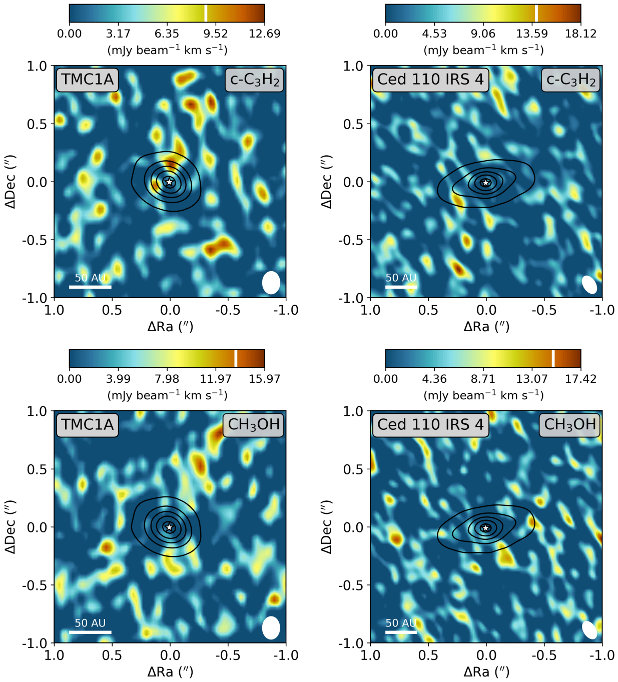

Figure 6.A.1: Integrated intensity maps of c-c_3H_2 $5_{2,3} - 4_{3,2}$ ($E_{\rm up} = 41.0$ K, top row) and CH_3OH $11_{0,11} - 10_{1,10}$ ($E_{\rm up} = 153$ K, bottom row) of TMC1A (left), IRS 4 (middle), and IRS 6 (right). The images are integrated over [-5,5] km s^{-1} with respect to the $V_{\rm lsr}$. The color scale is shown on the top of each image, where the white bar indicates the $3\sigma_{\rm line}$ level. The continuum flux is overplotted with the black contours at [0.1,0.3,0.5,0.7,0.9] times the peak continuum flux of 67.5, 17.3, and 2.5 mJy beam^{-1} for TMC1A, IRS 4, and IRS 6, respectively. The peak of the continuum emission is highlighted with the star. The size of the synthesized beam is displayed in the bottom right of each image and on the bottom left a scale bar is shown.

6.B Spectra of SO and SO2 for IRS 4 and IRS 6

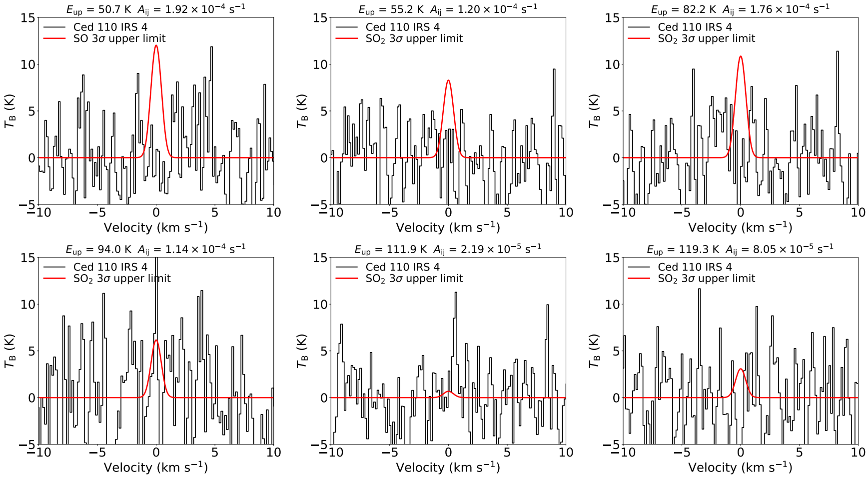

Figure 6.B.1: Spectrum of IRS 4 (in black) centered around the SO $6_5 - 5_4$ (top left) and five SO$_2$ transitions (other five panels). The $E_{\rm up}$ and $A_{\rm ij}$ of the corresponding transitions are reported on the top of each panel. None of the transitions are detected. The LTE model of the 3σ upper limit is overlayed on top in red.

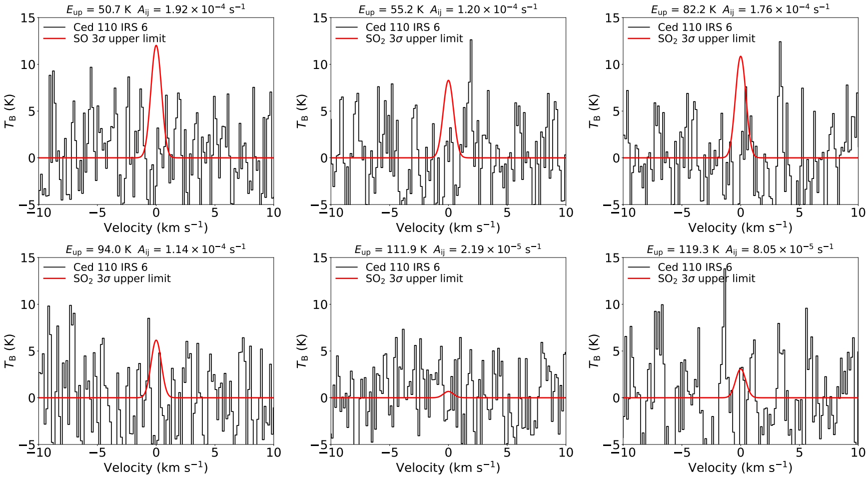

Figure 6.B.2: Spectrum of IRS 6 (in black) centered around the SO $6_5 - 5_4$ (top left) and five SO$_2$ transitions (other five panels). The $E_{\rm up}$ and $A_{\rm ij}$ of the corresponding transitions are reported on the top of each panel. None of the transitions are detected. The LTE model of the 3σ upper limit is overlayed on top in red.

6.C Additional tables

Table 6.C.1: Main observational properties of ALMA program 2021.1.01322.S.

Source	TMC1A	Ced 110 IRS 4	Ced 110 IRS 6
Configuration	C-6	C-7	C-7
Beam ($''$)	0.20×0.15	0.16×0.10	0.16×0.10
LAS ($''$)	2.0	1.5	1.5
ΔV (km s^{-1})	0.15	0.15	0.15
$\sigma_{\rm cont}$ (mJy/beam)	0.32	0.21	0.13
$\sigma_{\rm line}$ (K)	2.3	4.5	4.5

Table 6.C.2: Transitions of SO and SO_2 and isotopologues covered in the ALMA program 2021.1.01322.S. Only lines with $A_{\rm ij} > 10^{-6}$ and $E_{\rm up} < 1000$ K are included.

Species	Transition			Frequency	$A_{\rm ij}$	$E_{\rm up}$
	(J K L M	-	J K L M)	(GHz)	(s^{-1})	(K)
SO	2 1	-	1 2	236.4523	1.4×10^{-6}	15.8
	6 5	-	5 4	251.8258	1.9×10^{-4}	50.7
$S^{18}O$	6 5	-	5 4	232.2658	1.5×10^{-4}	47.8
SO_2	12 3 9	-	12 2 10	237.0688	1.1×10^{-4}	94.0
	15 2 14	-	15 1 15	248.0574	8.1×10^{-5}	119.3
	10 5 5	-	11 4 8	248.8308	2.2×10^{-5}	111.9
	13 1 13	-	12 0 12	251.1997	1.8×10^{-4}	82.2
	8 3 5	-	8 2 6	251.2106	1.2×10^{-4}	55.2
$^{33}SO_2$	31 9 23 29.5	-	32 8 24 30.5	232.0729	2.6×10^{-5}	650.5
	31 9 23 32.5	-	32 8 24 33.5	232.0729	2.6×10^{-5}	650.5
	31 9 23 30.5	-	32 8 24 31.5	232.0731	2.6×10^{-5}	650.5
	31 9 23 31.5	-	32 8 24 32.5	232.0732	2.6×10^{-5}	650.5
	4 2 2 4.5	-	3 1 3 3.5	232.4153	6.8×10^{-5}	18.8
	4 2 2 3.5	-	3 1 3 3.5	232.4156	1.0×10^{-5}	18.8
	4 2 2 3.5	-	3 1 3 2.5	232.4184	6.4×10^{-5}	18.8
	4 2 2 2.5	-	3 1 3 2.5	232.4193	1.0×10^{-5}	18.8
	4 2 2 4.5	-	3 1 3 4.5	232.4211	6.2×10^{-6}	18.8
	4 2 2 5.5	-	3 1 3 4.5	232.4222	7.4×10^{-5}	18.8
	4 2 2 2.5	-	3 1 3 1.5	232.4252	6.3×10^{-5}	18.8
	36 3 33 36.5	-	37 2 36 37.5	233.0263	1.8×10^{-6}	647.7
	36 3 33 35.5	-	37 2 36 36.5	233.0267	1.8×10^{-6}	647.7
	36 3 33 37.5	-	37 2 36 38.5	233.0363	1.8×10^{-6}	647.7
	36 3 33 34.5	-	37 2 36 35.5	233.0366	1.8×10^{-6}	647.7
	17 3 15 17.5	-	18 0 18 18.5	233.8339	1.4×10^{-6}	162.4
	17 3 15 16.5	-	18 0 18 17.5	233.8346	1.4×10^{-6}	162.4
	17 3 15 18.5	-	18 0 18 19.5	233.8428	1.4×10^{-6}	162.4
	17 3 15 15.5	-	18 0 18 16.5	233.8435	1.4×10^{-6}	162.4

Table 6.C.2: continued.

Species	Transition			Frequency	$A_{\rm ij}$	$E_{\rm up}$
	(J K L M	-	J K L M)	(GHz)	($\rm s^{-1}$)	(K)
$^{34}SO_2$	10 5 5	-	11 4 8	233.2964	1.8×10^{-5}	109.7
	5 2 4	-	4 1 3	235.9275	7.9×10^{-5}	23.2
	10 3 7	-	10 2 8	235.9519	1.1×10^{-4}	71.9
	20 2 18	-	19 3 17	236.2251	4.8×10^{-5}	207.2
	19 3 17	-	20 0 20	236.4288	1.4×10^{-6}	195.9
	13 1 13	-	12 0 12	248.6986	1.7×10^{-4}	81.8
	21 3 19	-	22 0 22	248.8557	1.5×10^{-6}	233.5
	9 3 7	-	9 2 8	250.3585	1.2×10^{-4}	62.6
	11 3 9	-	12 0 12	251.1766	1.0×10^{-6}	81.9
$SO^{18}O$	38 10 29	-	39 9 30	232.4605	2.8×10^{-5}	882.8
	38 10 28	-	39 9 31	232.4621	2.8×10^{-5}	882.8
	17 3 15	-	18 0 18	233.2785	1.4×10^{-6}	154.6
	5 2 4	-	4 1 3	233.4976	7.6×10^{-5}	22.6
	12 3 9	-	12 2 10	233.5884	1.1×10^{-4}	89.5
	6 2 5	-	5 1 4	248.0745	8.7×10^{-5}	27.8
	10 5 6	-	11 4 7	250.3455	2.2×10^{-5}	107.7
	10 5 5	-	11 4 8	250.3718	2.2×10^{-5}	107.7
	5 3 3	-	5 2 4	250.4810	1.0×10^{-4}	34.6
	37 10 28	-	38 9 29	251.1877	3.4×10^{-5}	849.8
	37 10 27	-	38 9 30	251.1887	3.4×10^{-5}	849.8
	7 3 5	-	7 2 6	251.2187	1.1×10^{-4}	45.9

Notes. All transitions and their characteristics are taken form the CDMS catalog (Müller et al. 2001, 2005; Endres et al. 2016).